*Proceedings of the*
*Annual Stability Conference*
*Structural Stability Research Council*
*Denver, Colorado, March 22-25 2022*

# Finite-element simulation of ductile crack propagation in steel structures

Andrew J. Ziccarelli[1], Xai Lao[2], Vincente Pericoli[3], Amit M. Kanvinde[4], Gregory G. Deierlein[5]

**Abstract**
A computational framework for simulating ductile crack propagation in steel structures was developed. This framework integrates an established model for the prediction of ductile fracture initiation under complex stress states (the Stress-Weighted Ductile Fracture Model) and the cohesive zone model for simulating the formation of new crack surfaces in continuum finite element analyses. Theoretical background and details on computational implementation will be discussed, along with methods for calibrating and validating the various model parameters. Results of coupon-scale experiments will be compared to complimentary finite element analyses to demonstrate the capabilities of the new model.

## 1. Background and Motivation

Fracture is a critical limit state in steel structures, which can lead to catastrophic failure of structural components. As such, understanding of the fracture process is crucial in order to maintain function of critical components in structures, so that global stability under extreme loads can be maintained. Fractures observed in steel structures after the 1994 Northridge and 1995 Kobe earthquakes underscore the importance of understanding the fracture process in the context of structural engineering.

Over the past three decades, aided by advances in computing power and structural analysis software, significant advancements have been made in the development of computational models which can predict the initiation of fracture in steel structures under complex stress states and loading conditions. While these models have proved useful, they are only capable of predicting the initiation of a ductile crack. Many full-scale structural tests have demonstrated that steel components can often withstand significant ductile crack growth before ultimate failure (Stojadinovic et al. 2000, Myers et al. 2009, Eatherton et al. 2013). The propagation of a ductile crack alters the continuum stress and strain fields within a component, and may have downstream impacts on global quantities (i.e. moment-rotation) or trigger brittle cleavage fracture. Models which can simulate this crack propagation are less well-developed, and represent a knowledge gap within the structural engineering community.

[1] Assistant Professor, North Carolina State University, <ajziccar@ncsu.edu>
[2] Graduate Research Assistant, University of California, Davis, <xlao@ucdavis.edu>
[3] Senior R&D Engineer, Sandia National Laboratories, <vperico@sandia.gov>
[4] Professor, University of California, Davis, <kanvinde@ucdavis.edu>
[5] Professor, Stanford University, <ggd@stanford.edu>

As performance-based designs, which rely upon an accurate simulation of structural response at extreme limit states including component failure and collapse, become more common, it is critical that computational tools are developed which can reliably simulate the propagation of ductile cracks in steel components. The work presented in the paper addresses this shortcoming by coupling an existing model for ductile fracture initiation with a framework for simulating crack propagation within finite element analyses. Theoretical background and implementation details are presented, followed by the results of an experimental testing program, which allowed for calibration and validation of the proposed framework.

## 2. Computational Framework for Simulating Ductile Crack Propagation

A computational framework for simulating crack propagation in structural steel must contain three essential components – (1) a rupture criterion (i.e., model for predicting fracture initiation), (2) a method for regularizing the stress and strain fields ahead of the sharp crack and (3) a method for simulating material separation within the finite element model. Details regarding the rupture criterion are presented in the following section. Afterwards, the theoretical background and implementation details of the model for crack propagation are presented.

### *2.1 Ductile Fracture Initiation*

Ductile fracture in structural steel is caused by microvoids which form within the steel matrix at second phase particles or inclusions. Voids nucleate by either particle-matrix decohesion or particle cracking. After a void has formed around an inclusion, it grows due to a combination of hydrostatic stress and plastic strain. Initially, voids may grow independently, particularly if the initial volume fraction of voids is low. However, adjacent voids will eventually interact with further growth. After a sufficient amount of void growth, a necking instability occurs in the ligament between voids. Finally, voids coalesce to form a macrocrack, which is observed as ductile fracture. This process is represented graphically in Fig. 1.

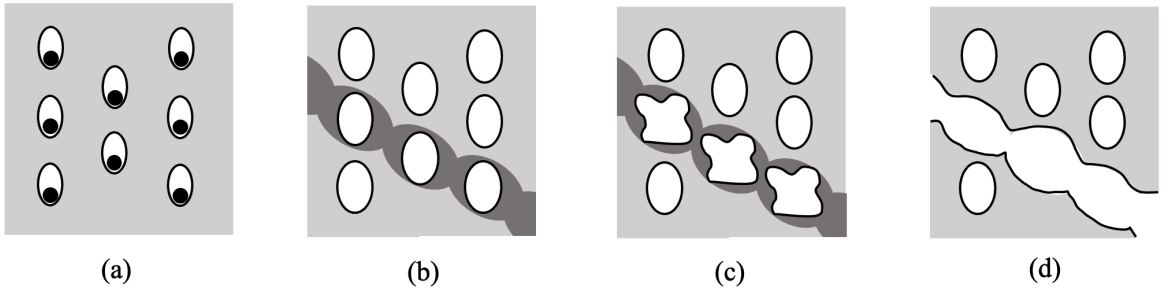


Figure 1: Stages of ductile fracture initiation: (a) void nucleation, (b) void growth and localization, (c) necking of ligament between voids and (d) void coalescence and fracture. Adapted from Anderson (2005).

Early attempts to mathematically describe the process of void growth in ductile metals are presented in by McClintock (1968) and Rice and Tracey (1969). In both cases, the authors derived equations which describe the growth of a single cylindrical or spherical void in an elastic-plastic material. Plastic strains were applied in the presence of triaxial stresses. Both indicate that the rate of void growth is related to the stress state – specifically, that void growth is exponentially related to the ratio of mean stress to yield stress. Rice and Tracey's expression for the rate of void growth, which forms the basis for many current models for ductile fracture, is given in Eq. 1:

$$\frac{dR}{R} = 0.283\left(2\sinh\left(1.5\frac{\sigma_m}{\sigma_y}\right)\right)\, d\bar{\varepsilon}_p \tag{1}$$

Where $R$ is the instantaneous void diameter, $\sigma_m$ is the mean stress, $\sigma_y$ is the yield stress and $\bar{\varepsilon}_p$ is the equivalent plastic strain. Later adaptations of this model substituted $\sigma_e$, the effective stress (or von Mises stress) for the yield stress, and substituted an exponential term for the hyperbolic sine term. The stress triaxiality ($T=\sigma_m/\sigma_e$) is an important parameter in the study of ductile fracture.

Over time, refinements to the model presented in Eq. 1 have been proposed to consider a variety of different loading conditions, including low-triaxiality, shear-dominated stress states and inelastic, cyclic loading conditions (Kanvinde and Deierlein 2007, Myers et al. 2014). Recently, Smith et al. (2021) presented a model for ductile fracture initiation termed the Stress-Weighted Ductile Fracture Model (SWDFM) which considers these two scenarios. The SWDFM has been extensively validated by several experimental datasets (Smith 2014 and Terashima 2018) covering a range of stress states and cyclic loading amplitudes. The model form of the SWDFM is given in Eq. 2:

$$D_{SWDFM} \;=\; C\int_{\varepsilon_p}\left[\exp(1.3T) - \frac{1}{\beta}\exp(-1.3T)\right]\exp(\kappa(|\xi|-1))\,\mathrm{d}\bar{\varepsilon}_p \text{ over } l \geq l^* \tag{2}$$

where $D_{SWDFM}$ is the damage index which ranges from 0 (no damage) to 1 (fracture initiation) and $\xi$ is the normalized Lode angle parameter, which is a measure of the variation of stresses within the deviatoric stress space which causes yielding. $C$, $\beta$ and $\kappa$ are material parameters. To ensure sufficient microstructural sampling, $D_{SWDFM}$ must be satisfied over a length $l$ greater than the characteristic length of the material, $l^*$, which is also considered a material parameter.

The SWDFM is calculated at each material point within a continuum finite element model. The damage index indicates the initiation of fracture at a given material point when the critical value of 1 is reached. However, this prediction of fracture is uncoupled from the simulation itself (i.e. the SWDFM does not impact the material constitutive or fracture response). Therefore, it must be coupled with another model which can simulate the physical effects of material separation and crack propagation within the finite element model.

*2.2 Adaptive Cohesive Zone Model for Simulating Crack Propagation*

Several existing numerical techniques are available to simulate crack propagation in a finite element model, including element extinction (Saykin et al. 2020), node release (Liu et al. 2019), cohesive zone models (Dugdale 1960, Barenblatt 1962, Camacho and Ortiz 1996) and phase field approaches (Bourdin et al. 2008). The cohesive zone model was selected to simulate crack propagation within the proposed framework, and was adapted to incorporate the ductile fracture model presented in Section 2.1 (see Pericoli et al. 2021 for further discussion).

The cohesive zone model relies upon cohesive finite elements, which are initially zero-width interface elements inserted in the finite element model along the plane of crack propagation. Cohesive elements utilize a uniaxial description of stress across the fracture plane, and behave according to a prescribed traction-separation relationship (TSR) which simulates the degradation of stress-carrying capacity as the material ruptures. The cohesive zone model was selected because

(1) cohesive elements provide regularization of the stress and strain fields ahead of the crack tip, avoiding the numerical singularity which is predicted by continuum theory and (2) the use of cohesive elements allows the fracture response to be simulated separately from the material constitutive response, thus allowing for the use of conventional elastic-plastic material models in continuum elements in simulations.

Many different traction-separation relationships have been proposed in the literature. The trilinear form for the TSR used in this framework is adapted from Tvergaard and Hutchinson (1992) and Cornec et al (2003), and is given in Eq. 3.

$$T = \begin{cases} k\Delta & \Delta < \Delta_1 \\ T_0 & \Delta_1 < \Delta < \Delta_2 \\ T_0\left(\frac{\Delta_u - \Delta}{\Delta_u - \Delta_2}\right) & \Delta_2 < \Delta < \Delta_u \end{cases} \tag{3}$$

Where $T$ is the traction (stress) carried by the cohesive zone element, $\Delta$ is the separation distance of the faces of the cohesive element, $k$ is the elastic stiffness, $T_0$ is the maximum stress capacity of the cohesive element, and $\Delta_1$, $\Delta_2$ and $\Delta_u$ are user-specified parameters which define the shape of the TSR.

In a conventional application of the cohesive zone model, the traction-separation relationship (i.e. Eq. 3) is prescribed a priori, and the maximum stress capacity of the cohesive element serves as the rupture criterion. However, in the proposed framework, termed the adaptive cohesive zone (ACZ) model, the traction-separation relationship of each cohesive zone element is adaptively set based on the value of $D_{SWDFM}$ in neighboring continuum elements. This is described graphically in Fig. 2.

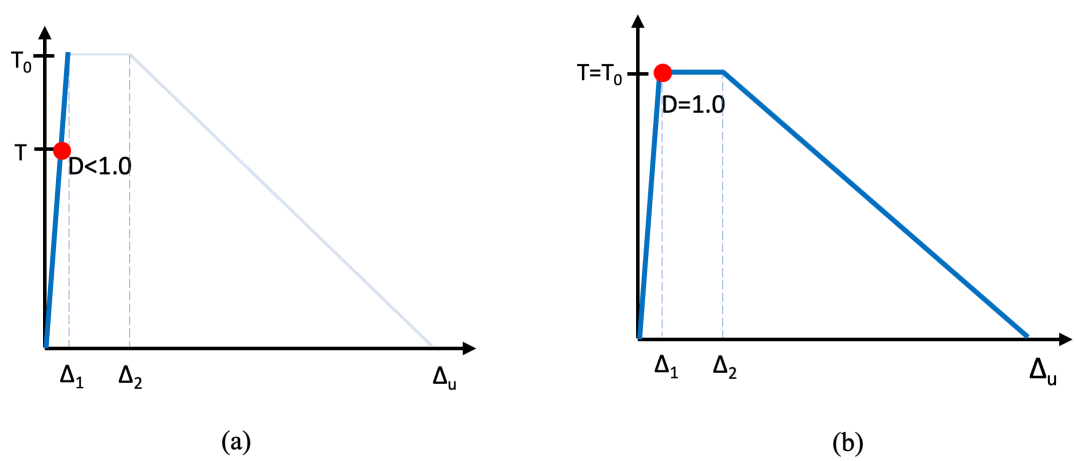


Figure 2: Cohesive traction separation relationship (a) prior to fracture initiation and (b) at fracture initiation

While the value of $D_{SWDFM}$ remains below the critical value of 1, fracture has not initiated, and the adaptive cohesive zone element remains on the initial (elastic) branch of the TSR. The maximum stress capacity of the element is set to an artificially high value in order to maintain this response. This is shown in Fig. 2(a). Once the value of $D_{SWDFM}$ reaches the critical value of 1 in neighboring

continuum elements (indicating fracture initiation), the maximum stress capacity of the adaptive cohesive element is set to the current level of stress carried by the element ($T=T_0$). The remainder of the TSR is established based on this value of $T_0$, and the user-defined values of $\Delta_1$, $\Delta_2$ and $\Delta_u$. Fig. 2(b) shows an example of the adaptively-set TSR.

As loading continues, the element follows the adaptively-set traction-separation relationship, until the maximum deformation capacity ($\Delta_u$) of the element is reached and stress is released (simulating an increment of crack extension). In this hybrid approach, the attractive features of the cohesive zone model are retained for simulating crack extension, while a strain-based index is integrated into the framework to indicate the initiation of ductile fracture, which would otherwise not be captured with a conventional cohesive model.

In addition, the adaptive traction-separation relationship may be modified to account for crack face closure under a reversal of loading, allowing for the simulation of crack extension under several successive loading cycles (Ziccarelli 2021). This is important when simulating the response of steel components which are subjected to earthquake loading. Fig. 3 shows the modifications to the TSR during cyclic loading. In Fig. 3(a), the response as the load reverses from tension to compression is shown. Upon re-loading in tension on the subsequent load cycle (Fig. 3(b)), the cohesive element follows a new load path, and the elastic branch TSR is oriented towards the peak displacement on the previous loading cycle.

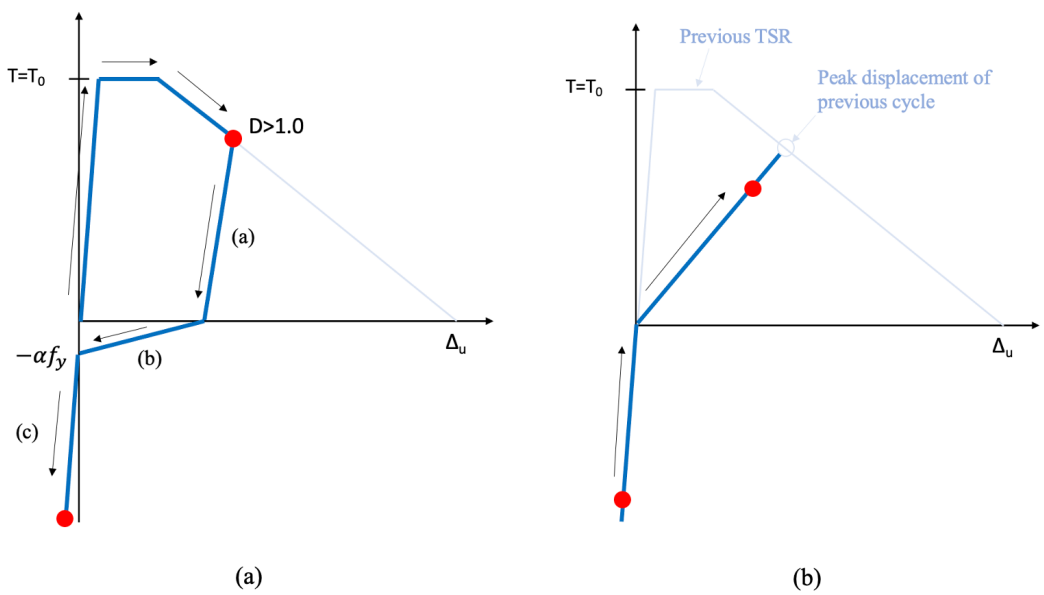


Figure 3: Cohesive traction separation relationship after fracture initiation under (a) compressive loading and (b) re-loading in tension on subsequent load cycle

The ACZ model was implemented into WARP3D (Healy et al. 2021), an open-source finite element program specifically designed for nonlinear fracture applications. Modifications were made to the cohesive zone material model and to the damage module, which calculates various fracture indices. In addition, a separate pre-processor was written which links each adaptive cohesive zone element with the appropriate neighboring continuum elements.

## 4. Calibration and Validation of Model with Coupon-Scale Experiments

*4.1 Experimental Specimens*

An experimental testing program consisting of 49 coupon-scale laboratory tests was conducted to provide data for calibration and validation of the ACZ model (Ziccarelli 2021). Specimens were designed to provide a range of stress states and tests were performed under both monotonic and cyclic loading protocols. Three primary specimen designs were used to provide data for calibration:

- *Cylindrical notched tension (CNT)* – CNT specimens are round tensile specimens which can be fabricated to provide a range of stress triaxiality values ($0.5<T<1.5$) by varying in notch radius ($R_N$). The stress state in the center of the bar is axisymmetric ($\xi$=1). CNT specimens are desirable because the point of fracture initiation is clearly evident from the global response (from the sharp change in stiffness of the force-displacement plot), allowing for straightforward data analysis for parameter calibration.
- *Grooved plate (GP)* – GP specimens are similar to CNT specimens, in that a range of triaxiality values may be provided by varying the notch radius ($0.9<T<1.3$), and fracture is easily observable from the global force-deformation plot. The difference is that the material in the center of the GP specimens is in a state of plane strain ($\xi$=0), which is in contrast to the CNT. This contrast provides data with which the parameter $\kappa$ in the SWDFM may be calibrated.

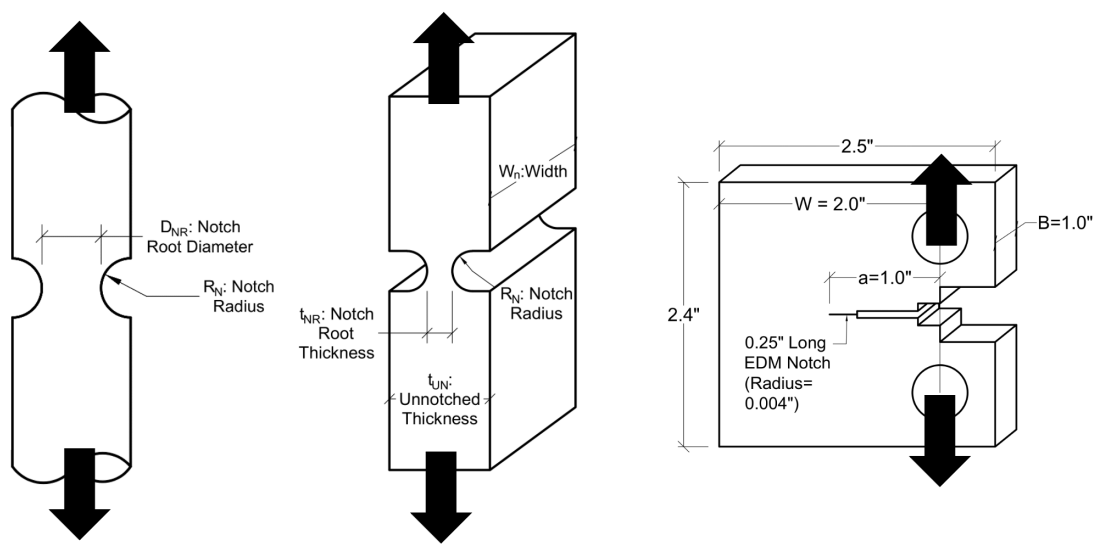


(a) (b) (c)

Figure 4: Experimental specimen designs – (a) Cylindrical Notched Tension, (b) Grooved Plate and (c) Compact Tension

- *Compact tension (CT)* – CT specimens are widely used with ductile metals to determine a material's resistance stable crack extension. Pins are placed through the specimen pin holes, and the specimen is loaded through displacement control of the pins. A ductile crack extends from the sharp pre-crack with applied displacement, and empirical formulas are used to monitor the extent of crack growth throughout the experiment. The J-integral (Rice

1968), which is a measure of the strain energy release rate per unit of crack extension, is also calculated throughout the experiment. CT specimens are fabricated with a V-shaped side groove on each side prior to testing, which provides a nearly-uniform stress state across the crack front.

*4.2 Finite Element Model Details*

For each experimental specimen, a complementary finite element model was constructed. In each case, adaptive cohesive elements were inserted into the finite element mesh along the crack plane. Figure 5 shows a typical finite element mesh for a CNT specimen, along with the adaptive cohesive elements. All finite element models utilized three-dimensional, 8-node linear "brick" elements, with the $\bar{\boldsymbol{B}}$ formulation (Hughes 1980) to reduce volumetric locking under fully plastic deformation.

CNT models were created with a single layer of elements, meshed in an angular slice (with angular dimension of one degree), to simulate axisymmetric conditions. Angular rotation was restrained through boundary conditions applied to each surface. Load was applied through displacement control of the top surface, while displacement of the bottom surface was held fixed. Total force carried by the specimen was recovered from the support reactions on the top surface of the specimen.

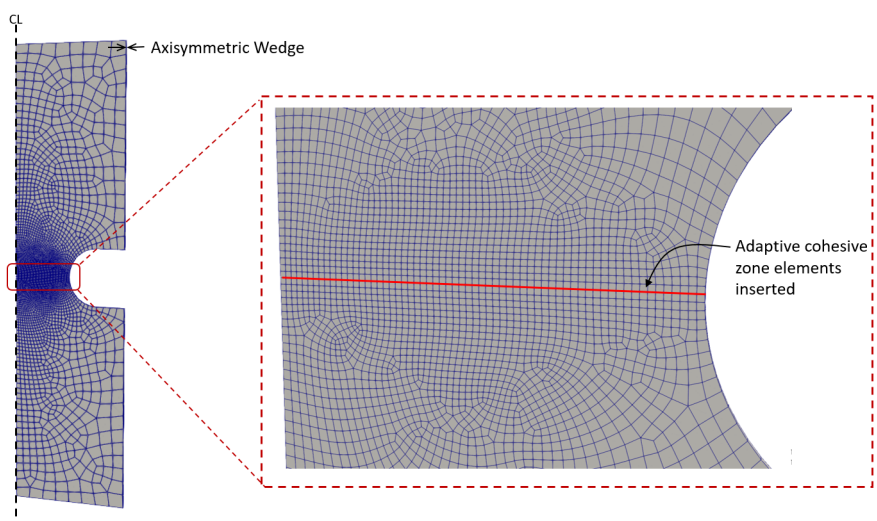


Figure 5: Finite element mesh for CNT with adaptive cohesive zone elements along crack plane

Three-dimensional grooved plate models were constructed, taking advantage of symmetry along two axes to reduce the model size. Load was applied through specified displacements of the top surface and the bottom surface was held fixed. Total force carried by the specimen was recovered from the support reactions on the top surface of the specimen.

Plane strain compact tension specimens were created with a single layer of elements, with out-of-plane constraint applied to both faces. Loading was applied through specified displacement of the nodes at the top and bottom of the appropriate loading holes. Load-line displacement was calculated by monitoring the displacement of the relevant nodes throughout the loading history. The J-integral was calculated using the domain integral procedure in WARP3D.

The material response was modeled with an elastic-plastic constitutive model with a von Mises yield criterion and combined isotropic and kinematic hardening. Isotropic hardening was modeled with an exponential model, and kinematic hardening was modeled with the Armstrong-Frederick model with two backstresses.

*4.3 Calibration of Model Parameters*

Five parameters were required to be calibrated based on the results of the experiments described in the previous section. Table 1 shows the parameters from each of the components of the framework to be calibrated. As discussed in Ziccarelli (2021), the parameters $k$, $\Delta_1$, and $\Delta_2$, which help to define the cohesive TSR, are specified by the user prior to calibration of the other parameters.

Table 1: Parameters to be calibrated

| Model | Parameter |
|---|---|
| SWDFM | $C$, $\beta$, $\kappa$, $l^*$ |
| ACZ | $\Delta_u$ |

A trial-and-error procedure was developed in which the parameters $C$, $\beta$, and $\kappa$ were calibrated to preliminary values based on the results of the CNT and GP tests, and then the CT tests were used to provide feasible values of $l^*$ and $\Delta_u$. Subsequently, simulations were run with each combined trial set of parameters ($C$, $\beta$, $k$, $l^*$, $\Delta_u$), and the set which minimized the error between the simulated results and the experimental results was taken as the calibrated parameter set.

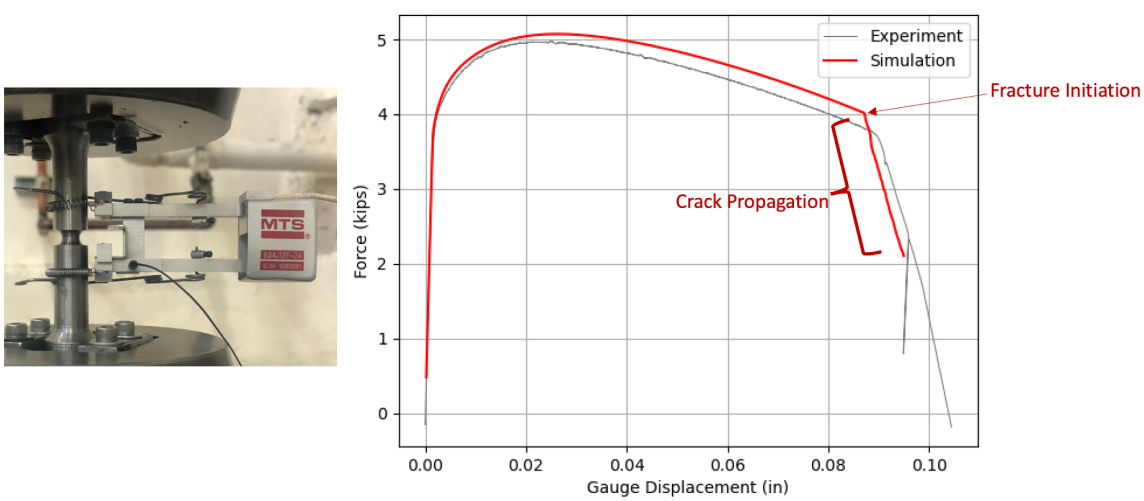


Figure 6: Force-displacement plot for experimental CNT specimen and corresponding finite element simulation

Results from a selected experiment and a simulation with the calibrated set of parameters are shown in Fig. 6. For the CNT experimental specimen in Fig. 6, a sharp change in stiffness is observed at a gauge displacement of 0.09 inches, indicating fracture initiation in the center of the specimen. As the crack propagates radially outward from the center of the bar, a steep drop-off in force is observed. Similar behavior is observed in the finite element simulation, with a sharp "kink" in the force-displacement plot at a displacement of approximately 0.085 inches, and a similar drop in force as the crack propagation was simulated.

*4.4 Validation with Blunt Notch Specimen*

After calibrating the model parameters, the final step was to validate the crack propagation framework with specimens that were not included in the calibration process. One of the specimens used to validate the ACZ framework was the Blunt Notch (BN) specimen. BN specimens are similar to CT specimens, with the primary difference being the geometry of the crack tip. Whereas CT specimens feature a sharp crack tip, blunt notch specimens feature a blunt, rounded tip (radius = 0.031 inches), which provides a different stress state ahead of the tip and allows for cyclic loading to be applied prior to fracture initiation. In addition, BN specimens are not side grooved, which provides a strong gradient in the stress state throughout the thickness of the specimen. Slight modifications to the calibration of the ACZ parameter $\Delta_u$ are made to account for three-dimensional effects, as discussed in Ziccarelli (2021).

A three-dimensional, half-symmetric finite element model was constructed to simulate the response of the BN specimens. The out-of-plane displacement at the middle of the specimen was constrained to account for symmetry and reduce model size. The model features 12 layers of elements in the through-thickness direction, with variable thickness to accurately capture the strong stress gradient which occurs near the edge of the specimen. Adaptive cohesive elements were inserted along the crack plane, as seen in Fig. 7.

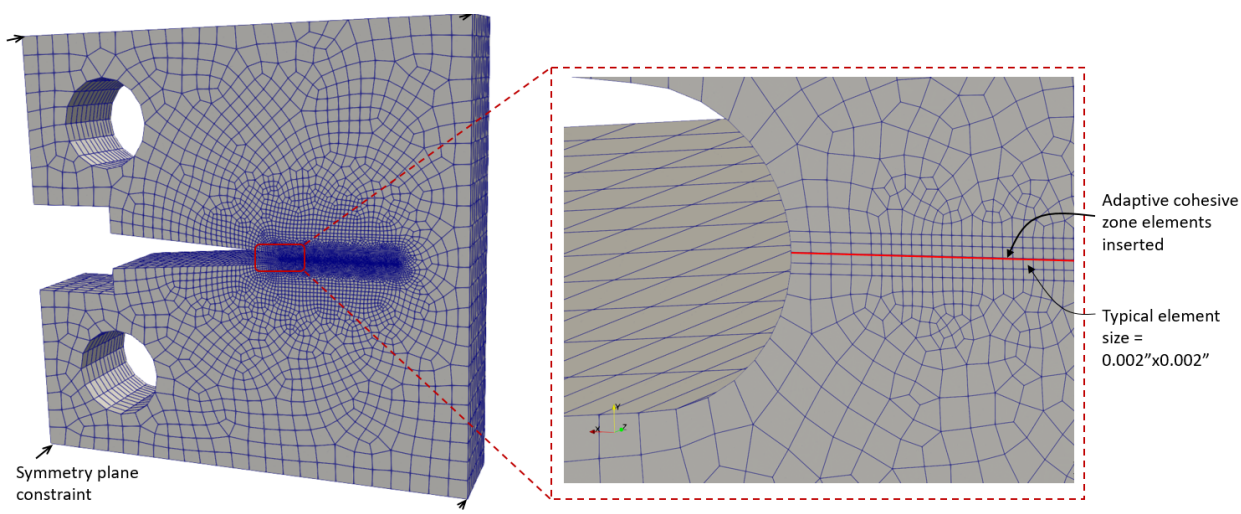


Figure 7: Finite element mesh for Blunt Notch specimen with adaptive cohesive zone elements along crack plane

A comparison of the simulated response and the experimental response for a monotonic BN specimen is shown in Figure 8(a). The simulation captures the overall response reasonably well, with minimal error in the peak force carried by the specimen between the simulation and the experiment. Furthermore, the similar slopes for the force-displacement plots indicate that the rate of crack propagation is well captured by the simulation. Figure 8(b) shows the shape of the simulated crack at the end of the analysis. A high degree of non-uniformity can be seen, with more rapid crack growth occurring at the center of the specimen and slower crack growth observed near the free surface. This was in line with experimental observations.

BN specimens were also tested with large-amplitude cyclic loading protocols. Since the fracture initiation model can predict fracture under both monotonic and cyclic loading conditions, and

because the ACZ model was formulated to include the effects of load reversals, the simulations were able to capture the response of the cyclic specimens, as well. This is significant for components subjected to earthquake loading.

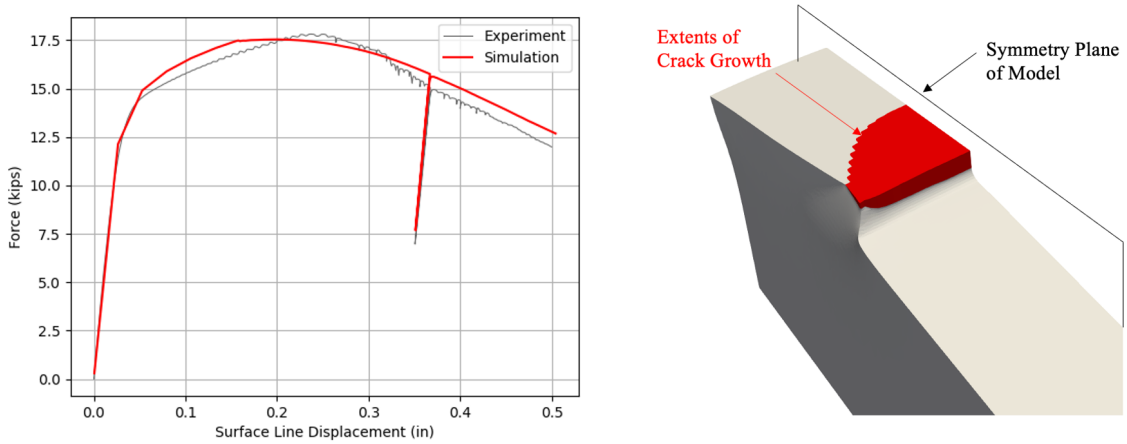


(a) (b)

Figure 8: Results from Blunt Notch finite element simulation: (a) force-displacement plot and (b) view of simulated crack shape at end of simulation

## 5. Conclusions

A computation framework for simulating ductile crack propagation in steel components was developed and implemented into a finite element program. This framework integrates an existing fracture initiation model with a model for simulating crack propagation, allowing for detailed post-fracture simulation of steel components. Model parameters were calibrated to the results of an experimental testing program consisting of 49 small-scale laboratory specimens, encompassing a range of stress states and loading protocols. Results of parameter calibration and model validation were presented, indicating good agreement between simulations and test data.

The implementation of this technology will allow for more accurate simulation of structural steel components under extreme loading. This will, in turn, allow for more accurate assessments of structural and component stability.

Despite the promising results, several limitations to the proposed framework exist and merit future study. The results presented consist primarily of mode-I (tension-dominated) fracture behavior, and further refinements to the framework may be required for more shear-dominated loading scenarios. Additionally, the proposed framework only considers ductile fracture and subsequent crack propagation, while ultimate failure in steel components often occurs due to brittle cleavage fracture, with ductile tearing as a precursor. The ACZ model allows for detailed analysis of the evolving stress and strain fields at the propagating ductile crack tip, which may then be utilized in conjunction with a model for cleavage fracture prediction to obtain a comprehensive fracture assessment.

## Acknowledgments

*This report is based upon collaborative research supported by the National Science Foundation (CMMI Award #1634291 and #1635043). Any opinions, findings and conclusions or recommendations expressed in this material are those of the author and do not necessarily reflect the views of the National Science Foundation. Additional laboratory support was provided by the John A. Blume Earthquake Engineering Center at Stanford University. The steel material utilized in this project was donated by Herrick Steel. The authors would also like to acknowledge Professor Robert Dodds (University of Tennessee), Christopher Smith (Berkshire Hathaway Specialty Insurance) and Masao Terashima (Nippon Steel) for their contributions.*

## References

Anderson, T. L. (2005). *Fracture Mechanics: Fundamentals and Applications.* Third Edition. Boca Raton, FL: CRC Press

Barenblatt, G. I. (1962). "The Mathematical Theory of Equilibrium of Crack in Brittle Fracture." *Advances in Applied Mechanics*, 7, 55–129.

Bourdin, B., Francfort, G. A., & Marigo, J. J. (2008). "The variational approach to fracture." *Journal of Elasticity*, 91(1), 5-148.

Camacho, G. T., & Ortiz, M. (1996). "Computational modelling of impact damage in brittle materials." *International Journal of Solids and Structures*, 33(20-22), 2899-2938.

Dugdale, D. S. (1960). "Yielding of steel sheets containing slits." *Journal of the Mechanics and Physics of Solids*, 8, 100–104.

Eatherton, M. R., Toellner, B. W., Watkins, C. E., & Abbas, E. K. (2013). "The effect of powder actuated fasteners on the seismic performance of protected zones in steel moment frames." *Report No. CE/VPI-ST-13/05*

Healy et al. (2021). "WARP3D: 3-D Dynamic Nonlinear Fracture Analysis of Solids Using Parallel Computers" University of Illinois.

Hughes, T. J. (1980). "Generalization of selective integration procedures to anisotropic and nonlinear media." *International Journal for Numerical Methods in Engineering*, 15(9), 1413-1418

Kanvinde, A.M. & Deierlein, G.G. (2007). "Cyclic Void Growth Model to Assess Ductile Fracture Initiation in Structural Steels due to Ultra Low Cycle Fatigue". *Journal of Engineering Mechanics*, 133(6), 701-712.

Liu, T., Qian, X., Wang, W., & Chen, Y. (2019). "A node release approach to estimate J-R curve for single-edge-notched tension specimen under reversed loading." *Fatigue & Fracture of Engineering Materials & Structures*, 42(7), 1595-1608

McClintock, F. (1968). "A criterion for ductile fracture by the growth of holes". *Journal of Applied Mechanics*, 35, 363-371.

Myers, A. T., Deierlein, G.G. & Kanvinde, A.M. (2009). "Testing and probabilistic simulation of ductile fracture initiation in structural steel components and weldments." *Blume Center Technical Report 170.*

Myers, A.T., Kanvinde, A.M., Deierlein, G.G. & Baker, J.W. (2014). "Probabilistic Formulation of the Cyclic Void Growth Model to Predict Ultralow Cycle Fatigue in Structural Steel". *Journal of Engineering Mechanics*, 140(6): 04014028

Pericoli, V., Lao, X., Ziccarelli, A., Kanvinde, A., & Deierlein, G. (2021). "Integration of an adaptive cohesive zone and continuum ductile fracture model to simulate crack propagation in steel structures." *Engineering Fracture Mechanics*, 258, 108041.

Rice, J.R. (1968). "A Path Independent Integral and the Approximate Analysis of Strain Concentration by Notches and Cracks". *Journal of Applied Mechanics*, 35, 379-386.

Rice, J.R. & Tracey, D. (1969). "On the Ductile Enlargement of Voids in Triaxial Stress Fields." *Journal of the Mechanics and Physics of Solids*, 17, 201-217.

Saykin, V. V., Nguyen, T. H., Hajjar, J. F., Deniz, D., & Song, J. (2020). "The effect of triaxiality on finite element deletion strategies for simulating collapse of full-scale steel structures." *Engineering Structures*, 210, 110364.

Smith, C. M., Deierlein, G., & Kanvinde, A. (2014). "A stress-weighted damage model for ductile fracture initiation in structural steel under cyclic loading and generalized stress states." *Blume Center Technical Report 187.*

Smith, C., Ziccarelli, A., Terashima, M., Kanvinde, A., & Deierlein, G. (2021). "A stress-weighted ductile fracture model for steel subjected to Ultra Low Cycle Fatigue." *Engineering Structures*, 245, 112964.

Stojadinović, B., Goel, S. C., Lee, K. H., Margarian, A. G., & Choi, J. H. (2000). "Parametric tests on unreinforced steel moment connections." *Journal of Structural Engineering*, 126(1), 40-49.

Terashima, M. (2018). “Ductile fracture simulation and risk quantification of Buckling-Restrained Braces subjected to Earthquakes” (Doctoral dissertation, Stanford University).
Ziccarelli, A. (2021). “Simulating earthquake-induced ductile crack propagation and brittle fracture in steel structures” (Doctoral dissertation, Stanford University).